Satellite observations of the water vapor greenhouse effect and column longwave cooling rates: Relative roles of the continuum and vibration-rotation to pure rotation bands

Anand K. Inamdar and V. Ramanathan

Center for Clouds, Chemistry and Climate, Scripps Institution of Oceanography, University of California, San Diego, La Jolla, California, USA

Norman G. Loeb

NASA Langley Research Center, Hampton, Virginia, USA

Received 16 July 2003; revised 25 January 2004; accepted 6 February 2004; published 20 March 2004.

[1] The Clouds and the Earth's Radiant Energy System (CERES) instrument on board the Tropical Rainfall Measuring Mission (TRMM) satellite provides, for the first time, a large-scale (40 S to 40 N) data set for the atmospheric greenhouse effect and the column-averaged longwave (LW) radiative cooling rates in the broadband (5–100 microns) and the window (8–12 microns) regions. We demonstrate here that the separation into the window and the nonwindow (5–8 microns and 12–100 microns) fluxes provides the first global-scale data set to exhibit the sensitivity of the atmospheric greenhouse effect to vertical water vapor distribution. The nonwindow greenhouse effect varies linearly with the logarithm of column water vapor amount weighted with the atmospheric pressure, while the window component varies quadratically with the water vapor partial pressure. The column cooling rates range from about -170 to -210 W m^{-2} for the nonwindow region. The window cooling rates are only about 10% to 20% of the above range and approach rapidly to near-zero values for surface temperatures less than 288 K. The nonwindow component of the greenhouse effect and cooling rates are shown to be more sensitive to upper troposphere water vapor, while the window greenhouse effect and cooling rates are shown to be more sensitive to the lower troposphere water vapor amount. In addition, the data reveal that in tropical regions, with warm sea surface temperatures (greater than 297 K) and elevated upper tropospheric water vapor amounts, the continuum emission in the window region leads to enhanced cooling of the column, while the rotational bands in the nonwindow region lead to a net decrease in the longwave cooling of the atmospheric column. *INDEX TERMS:* 1640 Global Change: Remote sensing; 1694 Global Change: Instruments and techniques; 3359 Meteorology and Atmospheric Dynamics: Radiative processes; 3314 Meteorology and Atmospheric Dynamics: Convective processes; *KEYWORDS:* remote sensing, instruments and techniques, radiative processes

Citation: Inamdar, A. K., V. Ramanathan, and N. G. Loeb (2004), Satellite observations of the water vapor greenhouse effect and column longwave cooling rates: Relative roles of the continuum and vibration-rotation to pure rotation bands, *J. Geophys. Res.*, *109*, D06104, doi:10.1029/2003JD003980.

1. Introduction

[2] The CERES instrument has been on board the U.S./Japanese Tropical Rainfall Measuring Mission (TRMM) satellite since December 1997. The CERES instrument made radiation measurements in its three-channel broadband scanning radiometers between January and August 1998 before operational problems forced the instrument to be shut off. CERES radiometers represent an improved version of the Earth Radiation Budget Experiment (ERBE) design [*Wielicki et al.*, 1996] and provide a greatly improved top-of-atmosphere (TOA) flux accuracy. Unlike the redundant channel configuration of ERBE, CERES has a shortwave (0.2–5 microns), a total (0.2–100 microns), and a window channel (8–12 microns). The window channel has played an important role in the parameterizations that relate the TOA fluxes directly to the surface fluxes and is expected to improve the estimates of clear-sky longwave flux at the surface [*Inamdar and Ramanathan*, 1997]. Furthermore, the TOA longwave (LW) flux for the window channel provides us with a unique opportunity to separate the window channel fluxes (mostly due to continuum absorption) from the nonwindow channel fluxes in the 5–8 micron and the 12–100 micron regions (due mostly to pure rotational bands of H_2O longwave of 12 microns and

0148-0227/04/2003JD003980$09.00

the vibration-rotation bands of H_2O and other trace gas shortwave of 8 microns).

[3] Studies hitherto (*Raval and Ramanathan* [1989], *Stephens and Greenwald* [1991], etc.) have focused on the total atmospheric greenhouse effect (i.e., integrated over the entire longwave spectrum). Although measurements of broadband radiation commenced over 2 decades ago with the launch of the Nimbus 7, the accuracy of the measurements has been found lacking in detecting small changes in the radiation balance at the top-of-atmosphere (TOA) [*Harries*, 1997; *Slingo and Webb*, 1997]. It is well known that both the forcing and the response to increasing greenhouse gases are spectrally dependent [*Kiehl*, 1983]. While the spectral response to perturbations in water vapor, the key greenhouse gas, is additionally height dependent, considerable disparities exist on the variability of the vertical structure of the tropospheric water vapor itself. This is important since the issue of water vapor feedback hinges critically on the role of the vertical structure of variability in the water vapor distribution and the associated sensitivity of climate. Uncertainties related to the structure of variability of the tropospheric moisture, especially the upper troposphere, mask the actual sensitivity of the water vapor greenhouse effect to height-dependent changes in the concentration of water vapor. The published studies on identification of the physical processes that determine the vertical distribution of water vapor and the associated sensitivity of the outgoing long-wave radiation have been quite conflicting [e.g., see *Lindzen*, 1990; *Shine and Sinha*, 1991; *Spencer and Braswell*, 1997; *Schneider et al.*, 1999; *Allan et al.*, 1999].

[4] Part of the reason for the discrepancy has been the unavailability of reliable measurements in the upper troposphere to characterize this variability. Seasonal humidity changes [*Inamdar and Ramanathan*, 1998] derived from the NASA Water Vapor Project data [*Randel et al.*, 1996] reveal a nearly unchanged relative humidity level in the lower troposphere for the tropics whereas a significant moistening occurs in the middle to upper troposphere dominated by the deep convective regions of tropics. Satellite-based observations reveal middle to upper tropospheric moistening [*Rind et al.*, 1991] for deep convective regions for both temporal (summer-winter) and spatial (west Pacific versus east Pacific) scales. *Bates and Jackson* [2001], using satellite radiance observations for a 20-year period, show evidence of upper tropospheric moistening in the monsoon regions and drying in the subtropical high regions. These results are also supported by the decadal-scale tropical humidity changes reported by *Hense et al.* [1988] and *Flohn and Kapala* [1989]. Other studies, especially those of *Schroeder and McGuire* [1998] and *Spencer and Braswell* [1997], along with that of *Lindzen et al.* [1995], suggested that the drying in the arid regions is so overwhelmingly large as to more than offset the moistening elsewhere. However, it is to be noted [*Soden and Schroeder*, 2000] that the tropical drying between 1988 and 1995 discussed by *Schroeder and McGuire* [1998] is apparently an artificial trend introduced because of a change in the radiosonde instrumentation. To resolve these issues, it becomes more essential to rely on direct observations of changes in the Earth's radiation budget as measured by satellites. However, simulation studies [*Mitchell et al.*, 1995; *Slingo and Webb*, 1997] show that broadband measurements at the top of the atmosphere yield too weak a signal to detect climate change. In this context, the CERES instrument with its window channel (8–12 microns), in addition to the broadband, offers us a unique opportunity to investigate the climate response to height-dependent forcings of humidity.

[5] Furthermore, it has been known for some time that the continuum absorption in the window plays a significant role in the atmospheric greenhouse effect [*Inamdar and Ramanathan*, 1994]. The present study examines the observational validity of this absorption. Not only do measurements of the window flux improve estimates of the surface longwave radiation budget [*Inamdar and Ramanathan*, 1997], but also the continuum absorption has been found to play a major role in the seasonal variation and latitudinal gradient of column longwave radiative heating and net surface LW radiative cooling. Other studies [*Sinha and Harries*, 1997; *Brindley and Harries*, 1998] have highlighted the importance of the far-infrared in climate change simulations. Results and inferences from all of the cited studies are based on model simulations. Although devoid of supporting observations, they do emphasize the need for a more precise evaluation of the spectral sensitivity of the longwave radiative budget supported by observations.

[6] This is the first time that an attempt has been made to investigate the effect of absorption in different parts of the water vapor spectrum on the atmospheric greenhouse effect on the basis of observations. It is to be emphasized here that the present study does not, per se, attempt to unravel the critical issue of water vapor feedback. The other supportive data fields used in this study are described in the next section followed by a partial validation of the CERES TOA fluxes employing the upper air data from the National Center for Atmospheric Research-National Meteorological Center (NCAR-NMC) data archive. An experiment is performed next to simulate the TOA window and nonwindow fluxes as measured by the CERES instrument, and we examine how they are influenced by changes in water vapor at different heights. Then we examine a subset of the water vapor profiles as measured by sondes over land stations and matched with CERES footprints to determine how the absorption in the window and nonwindow correlates with the measured humidity profile. The penultimate section, before the concluding remarks, is devoted to a discussion of the longwave radiative cooling rates in the window and nonwindow and how they can yield a signature on the transport and distribution of water vapor in the free troposphere.

2. Data

[7] The bulk of the data used in the present study, including some of the ancillary data products, comes from the CERES data system, produced and archived at the Langley Distributed Data Archive Center. The study also employs data from other sources, which are described later in the section.

2.1. CERES Data: LW Fluxes

[8] A distinctive feature of the CERES channel configuration is the presence of a spectral channel to measure the thermal radiation emitted from the Earth's surface in the 8–

12 micron "window" in addition to the total (0.2–100 μm) and shortwave (0.2–5 μm) channels. The improved angular and temporal sampling of the CERES scanner improves the accuracy of the data relative to ERBE by a factor of 2 to 3 [*Wielicki et al.*, 1996].

[9] CERES data are produced and archived by the CERES data analysis algorithm processes, which are formally grouped together in what are called "subsystems" (http://asd-www.larc.nasa.gov/ATBD/ATBD.html). The archival products from the subsystems fall into three major types of products: ERBE-like, surface and atmosphere products. The first outputs to be produced in the quickest time are the ERBE-like data products (data product referred to as ES8), which make use of the readily available ERBE algorithms. The scene-ids employ only the broadband radiance data. The angular distribution models (ADM) used for converting from radiance to flux are based on the Nimbus 7 measurements. While these data are best suited for intercomparison studies with the ERBE time period, they lack the state-of-the-art improvements available from the present CERES instrument. In the present study, we employ the instantaneous radiometric data available from the Single Satellite Footprint (SSF) data product of CERES, which commands a significantly better calibration accuracy for the TOA fluxes. This is possible through better identification of scene ids using collocated high-spectral-resolution and high-spatial-resolution cloud imager radiance data from the same spacecraft. The size of the footprint is about 10 km for nadir view. The monthly and seasonally averaged data employed here have also been derived from the same source. In addition to the TOA fluxes, CERES data analysis algorithms also produce surface radiative fluxes in the three channels through the use of direct TOA to surface algorithms developed by the science team members (http://asd-www.larc.nasa.gov/ATBD/pdf_docs/r2_2/ceres-atbd2.2-s4.6.0.pdf). The TOA to surface algorithm [*Inamdar and Ramanathan*, 1997] that produces surface radiative fluxes in the longwave channels (window and nonwindow) and employed in this study is physically based. These surface fluxes have also been validated against measurements at the various surface ground sites and are archived in the SSF data.

2.2. Ancillary Data

[10] The subsystem known as Meteorology, Ozone and Aerosol (MOA) produces and archives meteorological and other parameters. These parameters are derived from sources external to the CERES, and are regridded to conform to the CERES footprint scale. These parameters are also available from the SSF data set.

[11] There are two surface temperature products that are available. The source for one of them is the six-hourly European Centre for Medium-Range Weather Forecasts (ECMWF) field [*Rabier et al.*, 1998]. The other one is the surface skin temperature derived from the 11 micron clear-sky imager radiances employing the MOA profiles of temperature and moisture. Since the present analysis is confined to the clear skies, and also the TOA-to-surface longwave algorithm uses the latter, the imager-based surface skin temperature has been the preferred choice, although both products are similar except at a few isolated desert locations. The broadband and window surface emissivities compiled from the study of *Wilber et al.* [1999] and included in the SSF data sets have been used to estimate surface emission over nonblack land surfaces.

2.3. Rawinsonde Data

[12] The validations and the other correlative scientific studies reported in this paper, make use of the sonde measurements obtained from the NMC upper air data archive at NCAR from the vast network of land stations around the globe for the period January–April 1998. These data have been quality checked before use following the procedure described in our earlier papers [e.g., *Inamdar and Ramanathan*, 1994]. Ideally, we would have preferred to use sounding data over the oceans. However, owing to insufficient number of samples available, we were restricted to the land regions.

2.4. TOVS Water Vapor

[13] The Television Infrared Observation Satellite (TIROS) Operational Vertical Sounder (TOVS) Pathfinder Path A project produced a multi-year global moisture field [*Susskind et al.*, 1997], derived from analysis of High-Resolution Infrared Sounder 2 (HIRS2) and Microwave Sounding Unit (MSU). We have employed the monthly averaged precipitable water data above 500 mbar in this study. The monthly averaged fields of upper tropospheric water vapor from TOVS have been compared with Special Sensor Microwave Water Vapor Profiler (SSM/T-2) measurements [*Sohn et al.*, 2003] and found to be in excellent agreement.

3. Validation

3.1. TOA Fluxes

[14] The validation procedure is straightforward. The atmospheric profiles are input to a radiative transfer model (this model is described in detail by *Inamdar and Ramanathan* [1997]) to obtain the top-of-atmosphere clear-sky longwave fluxes in the broadband and window. The sonde locations are then collocated with the corresponding clear-sky CERES pixels. The collocation criteria used were that the matching samples should lie in a box 0.25 degree latitude by 0.25 degree longitude and in a 6-hour time window of each other. As stated earlier, the validation was confined to the land stations, because of the inability to obtain adequate samples over the ocean collocated with the clear-sky CERES pixels. The possible sources of error introduced in the validation are as follows:

[15] 1. The first is specification of the true radiating temperature of the surface. The first level of sonde data has been employed as a proxy for the surface temperature in the radiative transfer model calculations. The sondes usually report the 1 m air temperature, and if this is different from the surface radiometric temperature, it could significantly affect the OLR. Further, the CERES pixel domain size is about 10 km at nadir and gets bigger for nonnadir viewing angles, and surface temperatures cannot be expected to be uniform over the full domain especially over land. We restrict comparison to data points where the SSF-retrieved surface skin temperature products do not differ from the corresponding sonde reports by more than 5 K in order to limit errors due to spatial inhomogeneities.

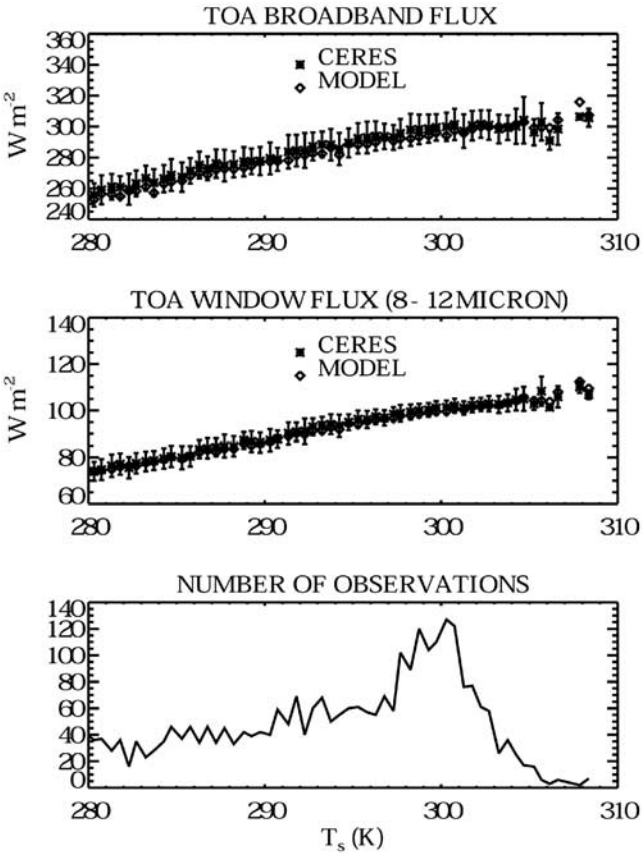

Figure 1. Comparison of CERES and model-simulated TOA longwave fluxes in the broadband and window for collocated data samples as a function of surface temperature. The vertical bars in the top two panels represent 1 standard deviation spread for the CERES measurements. The bottom panel shows the number of collocated data samples in each 0.5 K interval bin of surface temperature.

[16] 2. The second is upper tropospheric water vapor, which is most critical in determining the outgoing flux at TOA. Humidity measurements above 500 mbar are known for their poor quality [*Elliot and Gaffen*, 1991].

[17] 3. The third is scene identification. Although the scene ids based on the Visible Infrared Scanner (VIRS) imager data are known to be better than their ERBE counterpart, some uncertainties still cannot be ruled out.

[18] The validation results are presented in the form of CERES and model fluxes binned in 0.5 K intervals of surface temperature (Figure 1) and also as a scatterplot for broadband and window spectral regions (Figure 2).

3.2. Surface Fluxes

[19] The retrieval of surface LW fluxes from TOA CERES observed fluxes follows the empirical parameterization described by *Inamdar and Ramanathan* [1997] (and also see the ATBD document available through the web site http://asd-www.larc.nasa.gov/ATBD/ATBD. html). However, some significant changes have been implemented to the algorithms recently. Part of these changes are described in the quality summary document for TRMM CERES SSF Edition 2B products (http:// eosweb.larc.nasa.gov/PRODOCS/ceres/SSF/Quality_Summaries/ssf_surface_flux_trmm_ed2B.html). A full journal paper on the validation of surface LW fluxes is also being submitted soon. As shown by *Inamdar and Ramanathan* [1997], the window and nonwindow LW fluxes, along with surface and lower atmospheric temperatures can be used to estimate the surface LW fluxes. Thus the surface fluxes (at least the clear sky fluxes) are mostly based on observed data.

[20] Comparison of CERES-retrieved surface longwave fluxes with measurements at the Atmospheric Radiation Measurement (ARM) central and extended facility sites at Oklahoma Southern Grid Point are presented in Figure 3. The ARM sites represent one of the best instrumented sites available. The comparisons employ the 1-min measurements screened for clear-sky cases and encompass data from 21 different sites. As shown, both the mean and RMS errors are quite small.

4. Physics of the Window and Nonwindow Fluxes and Column Cooling Rates

[21] We consider two basic quantities: (1) G_a, which is the net reduction in the outgoing LW flux due to the presence of the atmosphere [*Raval and Ramanathan*, 1989] and is the difference between the upward flux at the surface and the TOA LW flux, and (2) G_a^*, the downwelling radiation emitted by the atmosphere to the

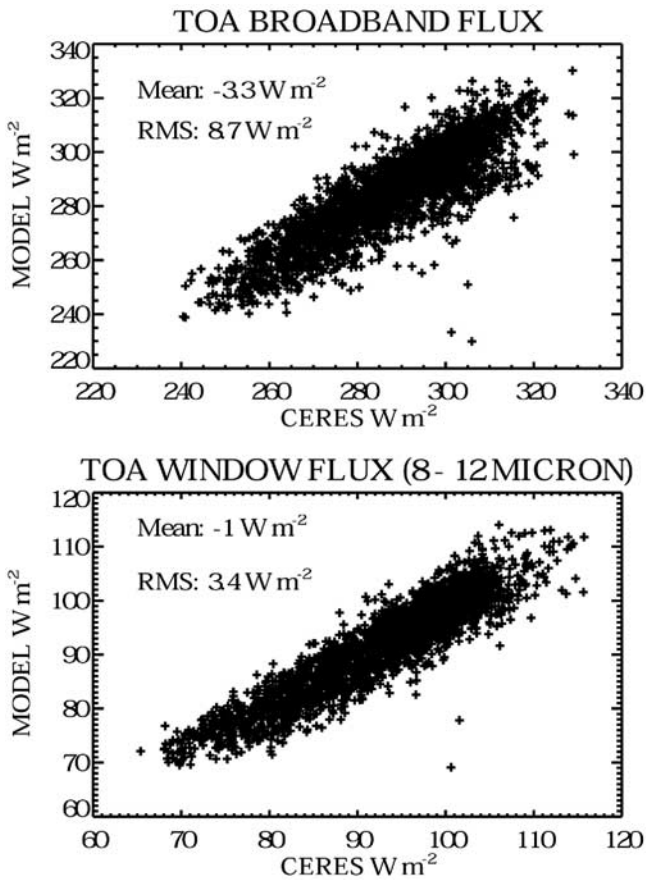

Figure 2. Scatterplot of CERES measurements and model results.

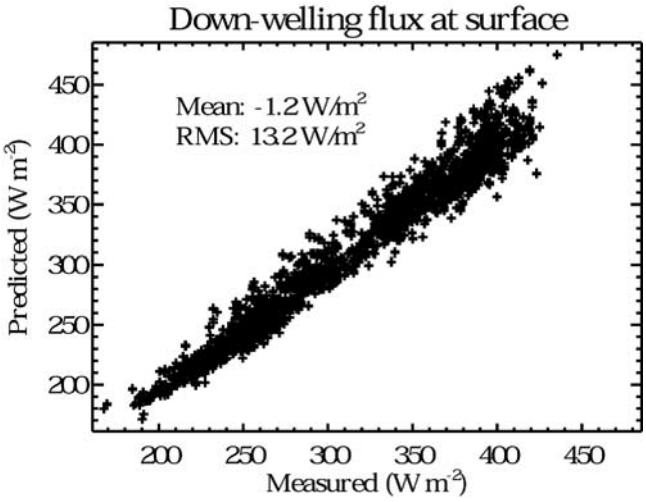

Figure 3. Comparison of instantaneous footprint-scale downwelling longwave flux retrieved from the CERES data analysis algorithms and in situ surface measurements at the ARM Central and Extended Facility sites.

surface. The difference between the two yields the column-integrated value for the divergence of the LW flux from the troposphere (***RC***), i.e., the LW cooling rate:

$$RC = G_a - G_a^*. \quad (1)$$

A negative value for ***RC*** (it is almost always negative) denotes LW cooling.

4.1. Sensitivity to Water Vapor Amount

[22] In order to understand the relative role of lower and upper troposphere water vapor in determining G_a and ***RC***, we will examine the sensitivity of G_a and G_a^* to changes in the vertical distribution of tropospheric water vapor. For this a typical tropical atmospheric profile has been chosen to simulate the broadband, window and nonwindow components of the longwave fluxes. We will examine the sensitivity per unit percentage change in the mass mixing ratio. The weighting functions $\partial \boldsymbol{G_a}/\partial \ln(\boldsymbol{w})$, $\partial(\boldsymbol{RC})/\partial \ln(\boldsymbol{w})$ are derived by averaging the sensitivity for perturbations of relative humidity (RH) ranging from 20% below the control value to 20% above the control value at each level, leaving the rest of the layers unperturbed. The term $\partial \ln(\boldsymbol{w})$ represents fractional change in precipitable water in a 20 mbar thick layer. As shown in Figure 4, $\boldsymbol{G_a}$ (broadband) is about equally sensitive to water vapor changes at all layers between 900 mbar and 300 mbar (Figure 4), with a slight maxima at 850 mbar and 300 mbar. However, this near-uniform sensitivity is due to the strong sensitivity of the window region in the lower troposphere between 900 mbar and 700 mbar and the strong sensitivity of the nonwindow region between 600 mbar and 300 mbar. The quadratic dependence of the window absorption (the so-called continuum absorption) on water vapor partial pressure ($\boldsymbol{e_w}$) is the main reason for the strong sensitivity of window fluxes to lower troposphere humidity. The nonwindow on the other hand is influenced

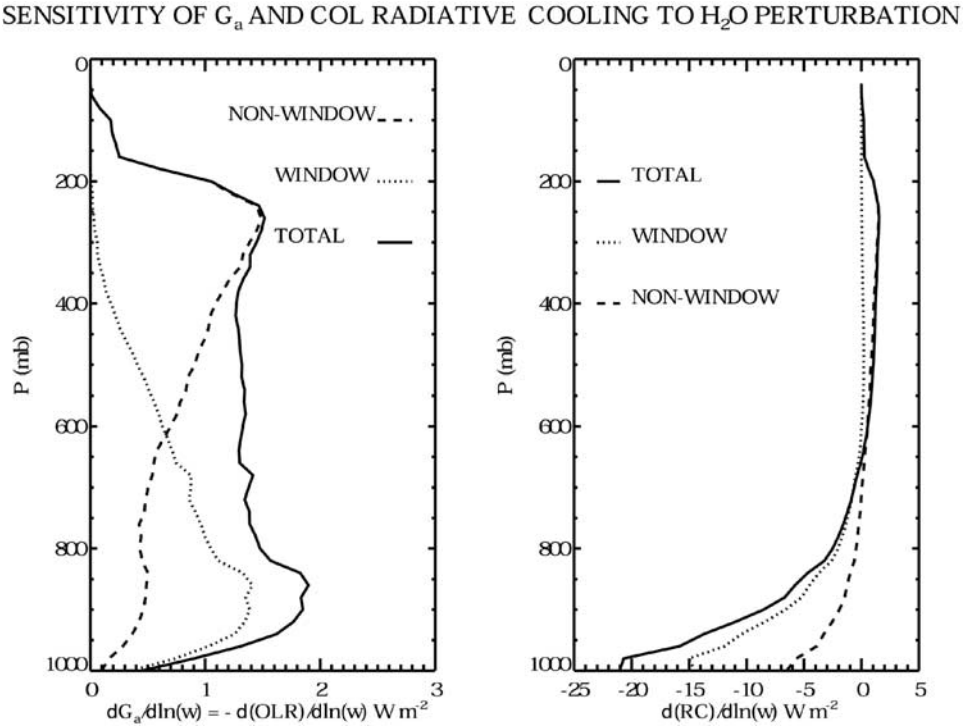

Figure 4. Sensitivity of the atmospheric greenhouse effect (left panel) and column radiative cooling (right panel) for a standard tropical atmospheric profile to height-dependent perturbations in water vapor. The weighting functions, $\partial \boldsymbol{G_a}/\partial \ln(\boldsymbol{w})$, $\partial(\boldsymbol{RC})/\partial \ln(\boldsymbol{w})$, shown separately for the total (solid line), window (dotted line), and nonwindow (dashed line), represent the change in the respective total column $\boldsymbol{G_a}$ or ***RC*** to a unit percentage change in the layer precipitable water.

more by the middle to upper troposphere water vapor content (Figure 4), because its optical depth is very large in the lower troposphere and hence its absorption is nearly saturated in the lower troposphere.

[23] The sensitivity of the column radiative cooling, $\partial(\boldsymbol{RC})/\partial\ln(\boldsymbol{w})$ (right panel of Figure 4), is even more interesting. The increase in the lower troposphere cooling rates due to the increase in water vapor is mostly due to the window region (again due to the quadratic dependence of absorption on $\boldsymbol{e_w}$), whereas increases in the upper troposphere humidity actually lead to a decrease in radiative cooling, i.e., positive sensitivity parameter, because of the strong absorption by the pure rotation bands of water vapor.

4.2. Dependence of G_a on Effective Column Water Vapor Amount

[24] The equation for, $\boldsymbol{G_a}$, in terms of the monochromatic absorptivity $\boldsymbol{A_\nu(z_{top}, z)}$ between the top of the atmosphere ($\boldsymbol{z_{top}}$) and altitude $\boldsymbol{z}$, is given by the integral form of the solution to the equation of radiative transfer, as

$$\boldsymbol{G_a} = \int_0^\infty \boldsymbol{d\nu} \int_{z_{top}}^0 \boldsymbol{A_\nu}\left(z_{top}, z'\right) \frac{\boldsymbol{dB_\nu}(z')}{\boldsymbol{dz'}} \boldsymbol{dz'}, \tag{2}$$

where $\boldsymbol{\nu}$ is the wave number in cm^{-1}. Thus $\boldsymbol{G_a}$ is an integral measure of the Planck function weighted column absorptivity for the atmosphere and thus a fundamental parameter. Contribution to this absorptivity comes from H_2O, CO_2, O_3 and many other trace gases. However, spatial and temporal variations in $\boldsymbol{G_a}$ are dominated by the variations in H_2O and temperature. In the nonwindow region, water vapor absorption (or more appropriately the optical depth) is largely governed by the water vapor amount weighted by the total atmospheric pressure as follows:

$$\tilde{\boldsymbol{w}} = (1/\boldsymbol{g}) \int \boldsymbol{q}\, \boldsymbol{p} \boldsymbol{dp}, \tag{3}$$

where $\boldsymbol{q}$ is the water vapor mass mixing ratio, $\boldsymbol{p}$ is the atmospheric pressure and $\boldsymbol{g}$ is the gravitational acceleration constant. The weighting with $\boldsymbol{p}$ represents the fact that the rotational lines are strong (i.e., opacity is very large at the line centers) and thus increase in absorption is mainly through the wings of the Lorentzian lines, which are pressure-broadened [*Cess*, 1974]. Alternately, collisions between unlike molecules (foreign broadening) predominate [*Clough et al.*, 1992] in broadening the rotational lines, and the line width depends on the total molecular population (i.e., on $\boldsymbol{p}$). In the window region, the continuum optical depth is determined largely by the water vapor amount weighted by the partial pressure of H_2O, $\boldsymbol{e_w}$, and expressed as

$$\tilde{\boldsymbol{w}}_e = (1/\boldsymbol{g}) \int \boldsymbol{q} \boldsymbol{e_w}\, \boldsymbol{dp}, \tag{4}$$

where the water vapor partial pressure, $\boldsymbol{e_w}$ is related to $\boldsymbol{q}$ and $\boldsymbol{p}$ as

$$\boldsymbol{e_w} = \boldsymbol{q}\, \boldsymbol{p}/0.622. \tag{5}$$

Thus it is obvious from equations (4) and (5) that $\tilde{\boldsymbol{w}}_e$ has a quadratic dependence on $\boldsymbol{e_w}$ and this quadratic dependence denotes the effects of self broadening of the far wings of rotational lines [*Clough et al.*, 1992]. It is to be noted, however, that although the continuum absorption extends outside the window, the quadratic dependence on water vapor partial pressure is true only for the dominant continuum in the window (8–12 microns). The correlation of nonwindow and window components of the atmospheric greenhouse effect against the appropriate absorber amounts, equations (3) and (4) evaluated for $\tilde{\boldsymbol{w}}$ and $\tilde{\boldsymbol{w}}_e$ respectively, are shown in Figure 5, employing the same set of collocated data points used for the TOA validation in section 3.1. For the nonwindow region, we plot $\boldsymbol{G_{a,nw}}$ against the logarithm of $\tilde{w}$ because the lines are strong and saturated and hence absorption increases logarithmically with the absorber amount [*Cess and Lian*, 1976]. As seen in Figure 5, $\boldsymbol{G_{a,nw}}$ for the nonwindow indeed increases logarithmically with the effective H_2O amount (top panel) while the window absorption increases quadratically with water vapor partial pressure (bottom panel). This confirmation that the effective absorptivity of the atmosphere conforms to the well understood quantum mechanical physics of water vapor absorption is reassuring and also offers confidence in the new window and nonwindow data generated by CERES.

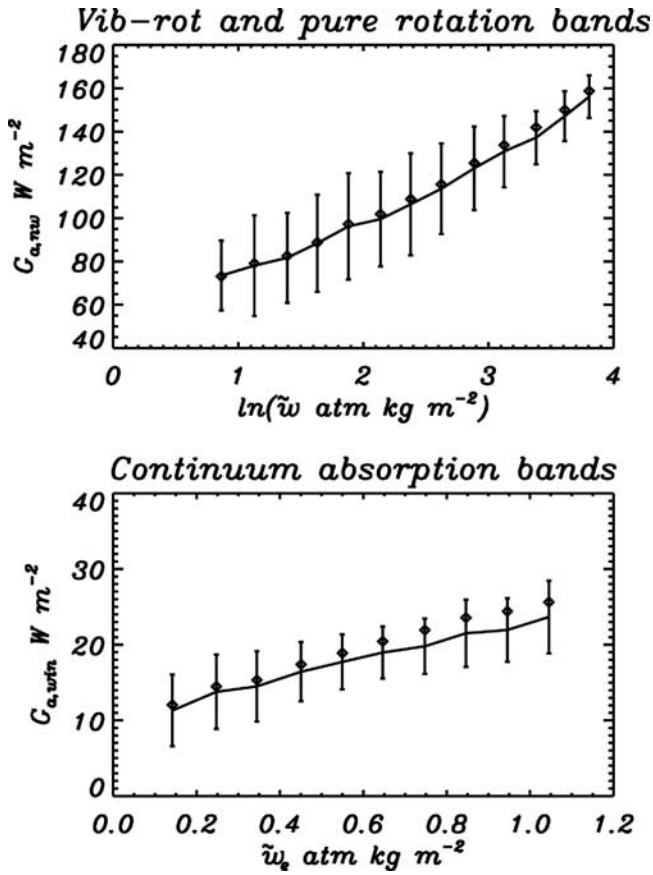

Figure 5. Observed atmospheric greenhouse effect components in the window and nonwindow plotted against the pressure-weighted precipitable water path lengths (see text). The same set of matched data pairs used in Figures 1–2 has been employed here.

5. Interactions Between Column Radiative Cooling, Surface Temperature, and Water Vapor

[25] Atmospheric column loses longwave radiative energy through both emissions at the TOA and emissions to the

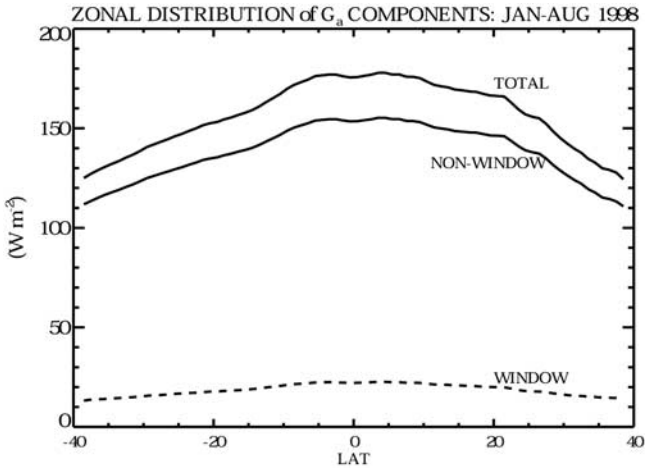

Figure 6. Seasonally averaged (January–August 1998) zonal distribution of the atmospheric greenhouse effect components.

surface. The radiative cooling term, ***RC***, introduced in section 4, captures the combined effect of these emissions. Each of the components of the radiative cooling term is sensitive to water vapor at different altitudes as shown in section 4. While the broadband G_a depends equally upon both the lower and middle to upper troposphere humidity, the nonwindow component of $\boldsymbol{G_a}$ is most sensitive to the upper troposphere, and the window component of $\boldsymbol{G_a}$ as well as G_a^* are influenced mostly by the lower tropospheric water vapor.

[26] Figure 6 depicts the zonal distribution of seasonally averaged (January–August 1998) G_a as obtained from the CERES measurements. The window component of G_a constitutes about 10% of the broadband and has a flatter response. The nonwindow component comprising the vibrational-rotational to pure rotational bands of water vapor tracks the broadband everywhere, as it contains the vast majority of the broadband thermal energy.

[27] Similarly, bulk of the column longwave radiative cooling (not shown) occurs in the nonwindow region. The contribution from the window channel to the net radiative cooling has significance only in the warm tropics (where surface temperatures, $\boldsymbol{T_s}$ exceed 295 K). The upper two panels of the scatterplots in Figure 7 summarize these features very well. The radiative cooling curves display 2 distinct temperature regimes representing the nonconvective (below 297 K) and convective (above about 297–298 K) regimes. The nonwindow cooling rate goes through a maxima (maximum cooling rate of -200 W m^{-2}) at about 297 K, and begins to decrease (less cooling) for $\boldsymbol{T_s} > 297$ K. Reverting to the results shown in Figure 4, which reveals that an increase in upper troposphere humidity leads to a decrease in LW cooling in the nonwindow region, we speculate that the behavior seen in Figure 7 (top panel) is due to an increase in the upper tropospheric humidity. To validate this point, we present the precipitable water above 500 mbar retrieved from the TOVS Pathfinder Path-A project collocated with the CERES footprints shown in the top two panels and averaged over the same period, in the bottom panel of Figure 7. The dynamics associated with convective regime [*Inamdar and Ramanathan*, 1994] contributes to the strong moistening shown in the bottom panel of Figure 7. This is also the same regime (in $\boldsymbol{T_s}$) experiencing the super greenhouse effect [*Raval and Ramanathan*, 1989] whereby an increase in $\boldsymbol{T_s}$ beyond 297 K, leads to an increase in $\boldsymbol{G_a}$ that exceeds that due to an increase in the black body surface emission. The rate of increase of downwelling radiation from the atmosphere to the surface is even larger explaining the sharp increase in the column radiative cooling in the window, which is dominated by the net flux divergence at the surface (middle panel of Figure 7). Thus these results provide observational confirmation of results from several previous studies based on models [*Stephens et al.*, 1994; *Cheruy and Chevallier*, 2000].

[28] In summary, the study of the partitioning of the longwave energy budget components in the continuum, vibrational-rotational and rotational bands as represented by the window and nonwindow components, and their sensitivity to height-dependent perturbations of moisture can be a very valuable tool in resolving the temporal and spatial variability of the atmospheric greenhouse forcing into pertinent information regarding the vertical transport and distribution of water vapor in the free troposphere.

6. Summary

[29] The present study reports on the new Earth radiation budget measurements made by the CERES instrument on

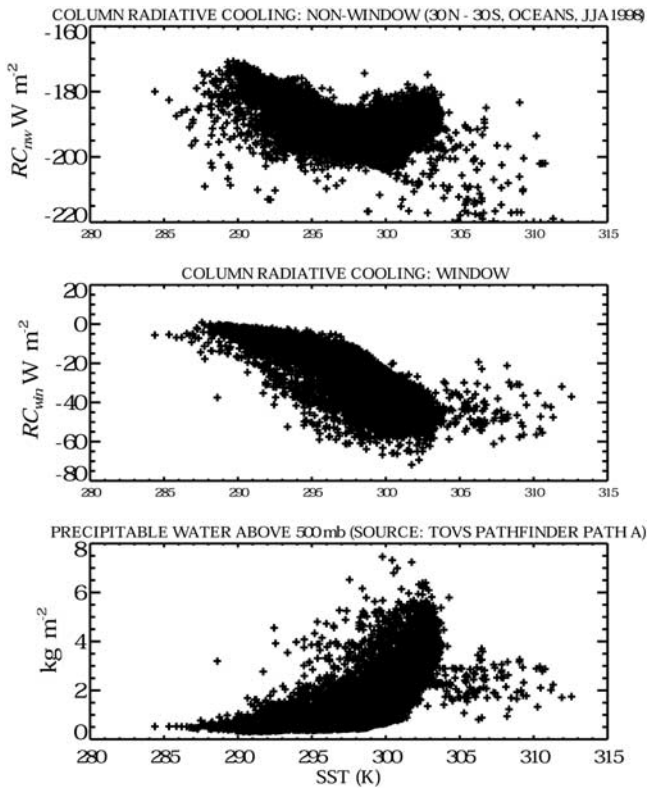

Figure 7. Column radiative cooling (***RC***) in the nonwindow and window channels (top two panels) inferred from the CERES observations and data for JJA 1998 over the ocean regions only. The bottommost panel shows the corresponding precipitable water above 500 mbar retrieved from the TOVS Pathfinder Path A project [*Susskind et al.*, 1997].

board the TRMM satellite during 1998. Well-calibrated, highly accurate TOA measurements, unique channel configuration and production, and archival of a comprehensive set of scientific data parameters have added a new dimension to the study of radiative budget measurements. We can obtain, for the first time, water vapor greenhouse effect split into contributions from the continuum (8–12 microns) and the vibration-rotation and pure rotation bands. Also retrieval of surface radiation budget directly from the TOA measurements using validated CERES data analysis algorithms has made it possible to obtain the clear-sky column radiative cooling, an important climate diagnostic parameter, over the globe without recourse to parameters describing the atmospheric state and their associated uncertainties.

[30] Model-based sensitivity studies reveal that while all layers of the troposphere contribute almost equally to the broadband greenhouse effect, the peak weighting for the contribution from the continuum or window channel occurs in the lower troposphere (around 850 mbar) and that the peak weighting for the vibrational-rotational water vapor absorption bands in the upper troposphere. Also continuum absorption contributes to enhanced radiative cooling in the lower part of the troposphere, while the vibration-rotation and pure rotation bands cause a slight heating (or a net decrease in the longwave cooling) of the atmospheric column for the nonwindow region relative to the window. The CERES observations also support the fact that the dominant continuum absorption (8–12 microns) varies quadratically with water vapor partial pressure consistent with theory. Thus while the pure rotational and vibrational-rotational bands in the nonwindow dominate the greenhouse effect and column cooling rates, the continuum (window) physics plays an important role in determining the latitudinal gradient of the longwave cooling rates. The results thus far are reassuring in that it confirms the well-known quantum mechanical physics of water vapor absorption and the physics of LW radiative cooling rates.

[31] Analysis of observational results to unravel the interactions between the greenhouse forcing parameters (G_a, G_a^*), surface temperature and tropospheric water vapor distribution reveals several interesting features. The window and nonwindow components of the longwave radiative cooling display contrasting patterns in the nonconvective and convective temperature regimes. Enhanced moisture in the upper troposphere and the associated strong absorption in the vibration-rotation and pure rotation bands results in reduced longwave cooling in the nonwindow component. At the same time, absorption in the dominant continuum wavelengths results in increased emissions to the surface contributing to the bulk of the enhanced net surface cooling. These results are fully consistent with the model sensitivity studies, and other satellite-based observations [*Rind et al.*, 1991].

[32] While the present study covers only eight months of CERES data, results suggest that examination of longer time series, including interannual changes could help in understanding the longer-term changes in greenhouse forcing and the implied pattern of changes in the distribution of tropospheric water vapor. The continuing EOS program with CERES instruments on board the TERRA and AQUA spacecraft with global coverage should provide more opportunities for such assessments.

[33] **Acknowledgments.** This work was supported by NASA/CERES grant NASA5-NAS1-98141. The authors wish to acknowledge the National Center for Atmospheric Research (NCAR) for providing access to the NCAR Scientific Computing Division's upper air data archive. Authors are also thankful to the anonymous reviewers, whose suggestions helped in greatly improving the quality of the paper.

References

Allan, R. P., K. P. Shine, A. Slingo, and J. A. Pamment (1999), The dependence of clear-sky outgoing long-wave radiation on surface temperature and relative humidity, *Q. J. R. Meteorol. Soc.*, *125*, 2103–2126.

Bates, J. J., and D. L. Jackson (2001), Trends in upper-tropospheric humidity, *Geophys. Res. Lett.*, *28*, 1695–1698.

Brindley, H. E., and J. E. Harries (1998), The impact of far IR absorption on clear sky greenhouse forcing: Sensitivity studies at high spectral resolution, *J. Quant. Spectrosc. Radiat. Transfer*, *60*, 151–180.

Cess, R. D. (1974), Radiative transfer due to atmospheric water vapor: Global considerations of the Earth's energy balance, *J. Quant. Spectrosc. Radiat. Transfer*, *14*, 861–871.

Cess, R. D., and M. S. Lian (1976), A simple parameterization for the water vapor emissivity, *J. Heat Transfer*, *98*, 676–677.

Cheruy, F., and F. Chevallier (2000), Regional and seasonal variations of the clear sky atmospheric longwave cooling over the tropical oceans, *J. Clim.*, *13*, 2863–2875.

Clough, S. A., M. J. Iacono, and J. L. Moncet (1992), Line-by-line calculations of atmospheric fluxes and cooling rates: Application to water vapor, *J. Geophys. Res.*, *97*, 15,761–15,785.

Elliot, W. P., and D. J. Gaffen (1991), On the utility of radiosonde humidity archives for climate studies, *Bull. Am. Meteorol. Soc.*, *72*, 1507–1520.

Flohn, H., and A. Kapala (1989), Changes in tropical sea-air interaction processes over a 30-year period, *Nature*, *338*, 244–245.

Harries, J. E. (1997), Atmospheric radiation and atmospheric humidity, *Q. J. R. Meteorol. Soc.*, *123*, 2173–2186.

Hense, A., P. Krahe, and H. Flohn (1988), Recent fluctuations of tropospheric temperature and water vapor content in the tropics, *Meteorol. Atmos. Phys.*, *38*, 215–227.

Inamdar, A. K., and V. Ramanathan (1994), Physics of greenhouse effect and convection in warm oceans, *J. Clim.*, *7*, 715–731.

Inamdar, A. K., and V. Ramanathan (1997), On monitoring the atmospheric greenhouse effect from space, *Tellus, Ser. B*, *49*, 216–230.

Inamdar, A. K., and V. Ramanathan (1998), Tropical and global scale interactions among water vapor, atmospheric greenhouse effect, and surface temperature, *J. Geophys. Res.*, *103*, 32,177–32,194.

Kiehl, J. T. (1983), Satellite detection of effects due to increased atmospheric carbon dioxide, *Science*, *222*, 504–506.

Lindzen, R. S. (1990), Some coolness concerning global warming, *Bull. Am. Meteorol. Soc.*, *71*, 288–299.

Lindzen, R. S., B. Kirtman, D. Kirk-Davidoff, and E. K. Schneider (1995), Seasonal surrogate for climate, *J. Clim.*, *8*, 1681–1684.

Mitchell, J. F. B., T. C. Johns, J. M. Gregory, and S. Tett (1995), Climate response to increasing levels of greenhouse gases and sulphate aerosols, *Nature*, *376*, 501–504.

Rabier, F., J. N. Thepaut, and P. Courtier (1998), Extended assimilation and forecast experiments with a four-dimensional variational assimilation system, *Q. J. R. Meteorol. Soc.*, *124*, 1861–1887.

Randel, D. L., T. H. Vonder Haar, M. A. Ringerud, G. L. Stephens, T. H. Greenwald, and C. L. Combs (1996), A new global water vapor dataset, *Bull. Am. Meteorol. Soc.*, *77*, 1233–1246.

Raval, A., and V. Ramanathan (1989), Observational determination of the greenhouse effect, *Nature*, *342*, 758–761.

Rind, D., E. W. Chiou, W. Chu, J. Larsen, S. Oltmans, J. Lerner, M. P. McCormick, and L. McMaster (1991), Positive water-vapor feedback in climate models confirmed by satellite data, *Nature*, *349*, 500–503.

Schneider, E. K., B. P. Kirtman, and R. S. Lindzen (1999), Tropospheric water vapor and climate sensitivity, *J. Atmos. Sci.*, *56*, 1649–1658.

Schroeder, S. R., and J. P. McGuire (1998), Widespread tropical atmospheric drying from 1979 to 1995, *Geophys. Res. Lett.*, *25*, 1301–1304.

Sinha, A., and J. E. Harries (1997), The Earth's clear-sky radiation budget and water vapor absorption in the far infrared, *J. Clim.*, *10*, 1601–1614.

Shine, K. P., and A. Sinha (1991), Sensitivity of the Earth's climate to height-dependent changes in the water vapour mixing ratio, *Nature*, *354*, 382–384.

Slingo, A., and M. J. Webb (1997), The spectral signature of global warming, *Q. J. R. Meteorol. Soc.*, *123*, 293–307.

Soden, B. J., and S. R. Schroeder (2000), Decadal variations in tropical water vapor: A comparison of observations and a model simulation, *J. Clim.*, *13*, 3337–3341.

Sohn, B. J., E.-S. Chung, J. Schmetz, and E. A. Smith (2003), Estimating upper-tropospheric water vapor from SSM/T-2 satellite measurements, *J. Appl. Meteorol.*, *42*, 488–504.

Spencer, R. W., and W. D. Braswell (1997), How dry is the tropical free troposphere? Implications for global warming theory, *Bull. Am. Meteorol. Soc.*, *78*, 1097–1106.

Stephens, G. L., and T. J. Greenwald (1991), The Earth's radiation budget and its relation to atmospheric hydrology: 1. Observations of the clear sky greenhouse effect, *J. Geophys. Res.*, *96*, 15,311–15,324.

Stephens, G. L., A. Slingo, M. J. Webb, P. J. Minnet, P. H. Daum, L. Kleinman, I. Wittmeyer, and D. A. Randall (1994), Observations of the Earth's radiation budget in relation to atmospheric hydrology: 4. Atmospheric column radiative cooling over the world's oceans, *J. Geophys. Res.*, *99*, 18,585–18,604.

Susskind, J., P. Piraino, L. Rokke, L. Iredell, and A. Mehta (1997), Characteristics of the TOVS Pathfinder Path A dataset, *Bull. Amer. Meteorol. Soc.*, *78*, 1449–1472.

Wielicki, B. A., B. R. Barkstrom, E. F. Harrison, R. B. Lee III, G. L. Smith, and J. E. Cooper (1996), Clouds and the Earth's Radiant Energy System (CERES): An Earth Observing System experiment, *Bull. Am. Meteorol. Soc.*, *77*, 853–868.

Wilber, A. C., D. P. Kratz, and S. K. Gupta (1999), Surface emissivity maps for use in satellite retrievals of longwave radiation, *NASA Tech. Pap., NASA TP 1999-209362*, 35 pp.

A. K. Inamdar and V. Ramanathan, Center for Clouds, Chemistry and Climate, Scripps Institution of Oceanography, UCSD, Mail Code 0221, La Jolla, CA 92093-0239, USA. (ainamdar@ucsd.edu; ram@fiji.ucsd.edu)

N. G. Loeb, NASA Langley Research Center, Mail Stop 420, 21 Langley Boulevard, Hampton, VA 23681-0001, USA. (n.g.loeb@larc.nasa.gov)